

Article

Ultrathin Cu(In,Ga)Se₂ Solar Cells with Ag/AlO_x Passivating Back Reflector

Jessica de Wild^{1,2,3,*}, Gizem Birant^{1,2,3} , Guy Brammertz^{1,2,3}, Marc Meuris^{1,2,3}, Jef Poortmans^{1,3,4,5} and Bart Vermang^{1,2,3}

- ¹ Institute for Material Research (IMO), Hasselt University (Partner in Solliance), Wetenschapspark 1, 3590 Diepenbeek, Belgium; Gizem.Birant@imec.be (G.B.); Guy.Brammertz@imec.be (G.B.); Marc.Meuris@imec.be (M.M.); jef.poortmans@imec.be (J.P.); bart.vermang@imec.be (B.V.)
- ² Institute for Materials Research in MicroElectronics (IMOMEC), Hasselt University IMEC (Partner in Solliance), Wetenschapspark 1, 3590 Diepenbeek, Belgium
- ³ Energyville, Thor Park 8320, 3600 Genk, Belgium
- ⁴ Interuniversity MicroElectronics Centre (IMEC) (Partner in Solliance), Kapeldreef 75, 3001 Leuven, Belgium
- ⁵ Department of Electrical Engineering, KU Leuven, Kasteelpark Arenberg 10, 3001 Heverlee, Belgium
- * Correspondence: Jessica.deWild@imec.be

Abstract: Ultrathin Cu(In,Ga)Se₂ (CIGS) absorber layers of 550 nm were grown on Ag/AlO_x stacks. The addition of the stack resulted in solar cells with improved fill factor, open circuit voltage and short circuit current density. The efficiency was increased from 7% to almost 12%. Photoluminescence (PL) and time resolved PL were improved, which was attributed to the passivating properties of AlO_x. A current increase of almost 2 mA/cm² was measured, due to increased light scattering and surface roughness. With time of flight—secondary ion mass spectroscopy, the elemental profiles were measured. It was found that the Ag is incorporated through the whole CIGS layer. Secondary electron microscopic images of the Mo back revealed residuals of the Ag/AlO_x stack, which was confirmed by energy dispersive X-ray spectroscopy measurements. It is assumed to induce the increased surface roughness and scattering properties. At the front, large stains are visible for the cells with the Ag/AlO_x back contact. An ammonia sulfide etching step was therefore applied on the bare absorber improving the efficiency further to 11.7%. It shows the potential of utilizing an Ag/AlO_x stack at the back to improve both electrical and optical properties of ultrathin CIGS solar cells.

Keywords: Cu(In,Ga)Se₂; ultrathin films; silver doping; AlO_x; passivation; optical enhancement



Citation: de Wild, J.; Birant, G.; Brammertz, G.; Meuris, M.; Poortmans, J.; Vermang, B. Ultrathin Cu(In,Ga)Se₂ Solar Cells with Ag/AlO_x Passivating Back Reflector. *Energies* **2021**, *14*, 4268. <https://doi.org/10.3390/en14144268>

Academic Editor: Lethy Krishnan Jagadamma

Received: 31 May 2021
Accepted: 9 July 2021
Published: 14 July 2021

Publisher's Note: MDPI stays neutral with regard to jurisdictional claims in published maps and institutional affiliations.



Copyright: © 2021 by the authors. Licensee MDPI, Basel, Switzerland. This article is an open access article distributed under the terms and conditions of the Creative Commons Attribution (CC BY) license (<https://creativecommons.org/licenses/by/4.0/>).

1. Introduction

Ultrathin Cu(In,Ga)Se₂ (CIGS) solar cells are being studied as an option for large-scale application of this technology. Thinner absorber layer reduces the amount of In (and Ga) required, and could speed up the processing time. When going to ultrathin absorber layers, losses due to incomplete absorption and recombination at interfaces needs to be compensated for. In the case of CIGS solar cells, electrical losses due to recombination at the CIGS/Mo interface can be reduced by applying a high Ga gradient or a di-electric passivation layer [1,2]. As di-electric, AlO_x has been widely applied and proven to reduce the recombination at this interface [3]. Optical losses can be reduced by increasing the path length of the longer wavelengths. This can be achieved by texturization-inducing scattering [4], reflective mirrors at the back, reflecting the light back into the solar cells [5] or even plasmonic coupling, enhancing the electromagnetic field locally [6].

Application of textured structures or reflective mirrors are commonly seen in thin film silicon. In the case of a standard CIGS absorber layer thickness, this was not required, as the absorption coefficient is high enough to absorb all the light. For ultrathin CIGS absorber layers, this is not the case anymore, and light management is required to absorb all the light. Most light management techniques have been applied at the CIGS/Mo interface, since the internal reflection between the CIGS and Mo layer is rather low, and causes parasitic

absorption losses. As the light management structures are generally placed at the CIGS/Mo interface, a technical difficulty is added in the choice of applicable optical structures. These applied structures should withstand the harsh environment in which CIGS layers are grown, which is usually in Se excess and at temperatures above 500 °C. Di-electrics and some transparent conductive oxides (TCO) withstand this environment well, and may increase the reflection and reduce the parasitic losses at the CIGS/Mo interface due to the change in the refractive index [7]. In combination with a metal, higher internal reflection is calculated and thus higher current generation [8]. Practically, current improvements are observed upon applying structured SiO_x islands [9,10], using metallic mirrors [10–12], TCO layers [13] and encapsulated Au nanoparticles [14]. These methods are based on advanced nano-lithography techniques, or rather thick metallic layers, making it expensive or difficult to upscale the methods. In addition, in most cases these optical improvements are counteracted by losses in fill factor (FF) and/or open circuit voltage losses (Voc) as the optimal CIGS/(MoSe₂)/Mo contact is negatively affected.

In this contribution, we studied the potential of using an Ag/AlO_x stack at the back of ultrathin CIGS solar cells to increase both the optical and electrical properties. Ag is used as it is known not to harm the CIGS layer properties. Silver replaces copper in the lattice, and does not introduce detrimental point defects. Additionally, due to the lower melting point of Ag-containing chalcogen, the crystallinity may improve when grown at the same temperature [15]. We will first study the effect of Ag incorporation, and secondly the application of an Ag/AlO_x stack. The thickness of the AlO_x layer was chosen in such a way that holes are formed during the CIGS growth in the presence of evaporated NaF. These holes are required to make electrical contact with the Mo at the back [16,17]. It is assumed that only after formation of the holes, the Ag diffuses into the CIGS layer. Lastly, ammonium sulfide treatment, which is a known etchant for removing copper selenide [18], was also performed. An efficiency increase from 7% to almost 12% was achieved due to both passivation and optical enhancement.

2. Materials and Methods

Ultrathin CIGS layers are grown by a three-stage co-evaporation process. As substrate, glass/Si(O,N)/Mo is used, in which the Si(O,N) layer suffices as an alkali barrier. The Na is added separately prior to the CIGS growth by NaF evaporation. To make ultrathin CIGS absorber layers, the same three-stage process as for thick (~2 μm) layers is used, with one small adaptation. During the temperature change to go from copper poor to copper rich, the shutters were closed. The shutter is opened again when the elemental fluxes are stable. This will result in a rather flat gallium profile, similar to the single stage process [19], although there was still a copper rich stage during the growth. The substrate temperature was set at 550 °C for all the stages. The final thickness was about 550 nm. During growth, a sample without Ag was added to measure the composition with XRF. For all samples, the average [Cu]/([Ga] + [In]) was ~0.8 and [Ga]/([Ga] + [In])~0.3.

The Ag layers were evaporated on the Mo substrates, and are 10 or 20 nm. A 3 nm thin AlO_x layer was grown on top of the Ag layer by atomic layer deposition (ALD) at 150 °C. Trimethylaluminum (TMA) was used as the Al precursor, and H₂O was used as a reactant. The samples were then placed in the co-evaporation chamber, and NaF was evaporated at room temperature. During the CIGS growth, the Na ions react with the AlO_x in the presence of Se, and holes in the AlO_x are formed [16,17]. The silver is assumed to diffuse through these holes into the CIGS layer. It is assumed that the Ag will not diffuse through the AlO_x layer itself, and thus remains below the AlO_x layer. The back contact will then consist of local CIGS/Mo contacts with Ag/AlO_x passivated areas. Furthermore, a sample without AlO_x was prepared as an Ag reference. A scheme of the different back contact approaches is presented in Figure 1.

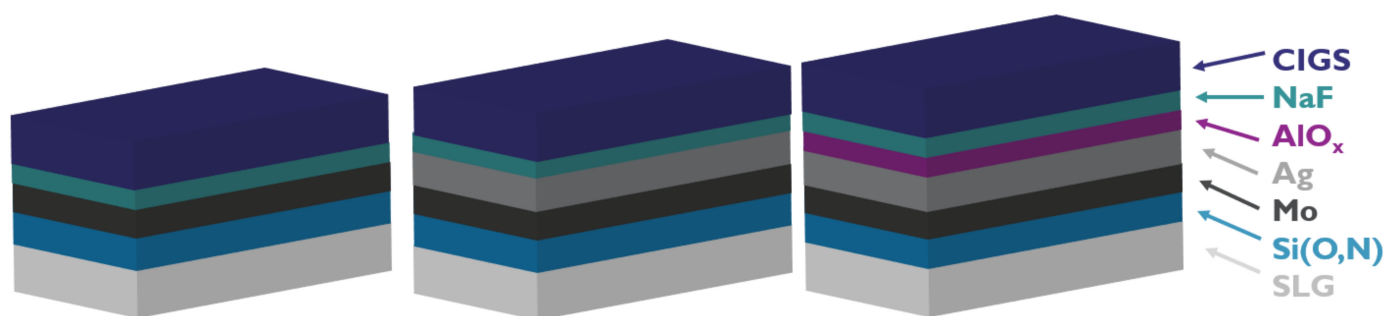


Figure 1. Schematic overview of the different samples: **(left)** standard CIGS layer on Mo; **(middle)** CIGS layer grown on 10 nm Ag; **(right)** CIGS layer grown on Ag/AIO_x stack. The AIO_x was 3 nm and the Ag layer 10 or 20 nm.

The samples were further processed into solar cells by chemical bath-deposited CdS, sputtered i-ZnO/aluminum-doped ZnO window layers and evaporated Ni/Ag/Ni grids. A second set of 10 nm and 3 nm AIO_x was prepared, of which one sample was etched and the other was further processed, as described above. The etching was performed in pure ammonia sulfide solution by immersing the sample for 10 minutes in the solution at room temperature. After washing the absorber layer in deionized water, the sample was further processed into a solar cell.

The cells were electrically characterized by current voltage (JV), and quantum efficiency (EQE) measurements. The solar cells were measured with a Keithley 2400 source meter using a four-point probe under A.M. 1.5 spectra. Per sample, at least six cells were measured. A part of the sample with the 20 nm Ag layer was shunted, and cells with FF below 30% were excluded from the analysis. EQE spectra of at least two cells were measured using a Bentham EQE setup with 10 nm resolution. The cells were further measured by photoluminescence (PL) and time resolved PL (TR-PL) using a picoquant 300 fluotime photospectrometer setup. The excitation wavelength was 532 nm, time resolution 25 ps and the repetition rate 3 MHz. Per sample, at least three spectra and TRPL decay curves were obtained. Time of Flight—Secondary Ion Mass Spectroscopy (ToF-SIMS) measurements were performed using ION.TOFS instrument (ION.TOFS GmbH, Muenster, Germany). Sputtering was carried out with a 2 keV O₂ ion beam. The sputter area of 350 × 350 μm², and an analysis area of 100 × 100 μm² was used for the depth profiles, with a raster of 128 × 128 pixels. 15 keV Bi⁺ was used as an analysis beam. Scanning electron microscopy (SEM) imaging and energy dispersive X-ray spectroscopy (EDS) analysis was done using a Tescan and Bruker SEM. The composition of the bare absorber layers was measured using a 20 kV electron beam. The top layers were removed by diluted HCl solution before the EDS measurement. The back contact was measured using a 10 kV electron beam, to be more surface sensitive. Diffuse and total reflection spectra of the bare absorber layers were measured with an integrating sphere using a Si (350–1100 nm) and Ge detector (1000–1400 nm). The spectra was measured between 350 and 1400 nm with 10 nm resolution. The system was calibrated with a reference reflection spectrum. With a Keyence confocal microscope, the line roughness was measured using 150× magnification.

3. Results

3.1. Opto-Electrical Characterization

The JV parameters of the Ag containing solar cells are presented in Figure 2. Additionally, an ultrathin three-stage baseline sample without Ag is presented. The solar cell with Ag only has similar performance as the three-stage cell without Ag. They have a Voc of ~585 mV, FF of ~56% and current of 20 mA/cm². The maximum efficiency is about 7%. It shows that the Ag itself is not harming the solar cell performance. This is consistent with reports about Ag incorporation into CIGS [20,21]. When the AIO_x is deposited on top of the Ag layer, all solar cell parameters improve (see the red and blue data). The increased Voc and FF are likely due to passivation. The current increase is about 2 mA/cm². In Figure 3, the EQE curves and tauc plots of the Ag-containing solar cells are presented. We

indeed found that the Ag/ AlO_x cells have a higher EQE response compared to the cell with Ag only. The integrated current densities were 24.3, 25.8, 26.1 mA/cm^2 for the 10 nm Ag without and with 3 nm AlO_x and 20 nm Ag/3 nm AlO_x , respectively. The increase in current is about 1.5–1.8 mA/cm^2 when there is also an AlO_x layer. This is more than observed in previous studies using only AlO_x , and we therefore believe that this is due to the Ag/ AlO_x stack [17,22]—this will be explored later on. From the tauc plots, we find that the band gaps are about 1.2 eV. These values are summarized in Table 1.

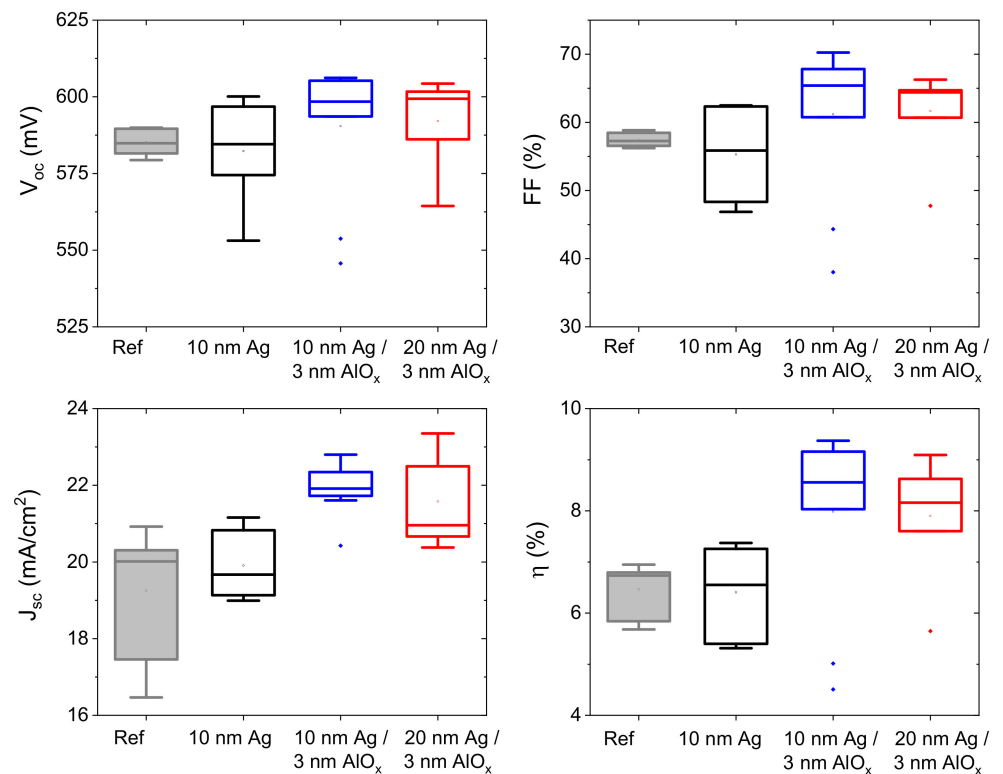


Figure 2. JV parameters of Ag-incorporated CIGS solar cells with and without AlO_x . Additionally, an ultrathin three-stage solar cell without Ag is presented. (Top left) V_{oc} ; (top right) FF; (bottom left) J_{sc} ; (bottom right) efficiency.

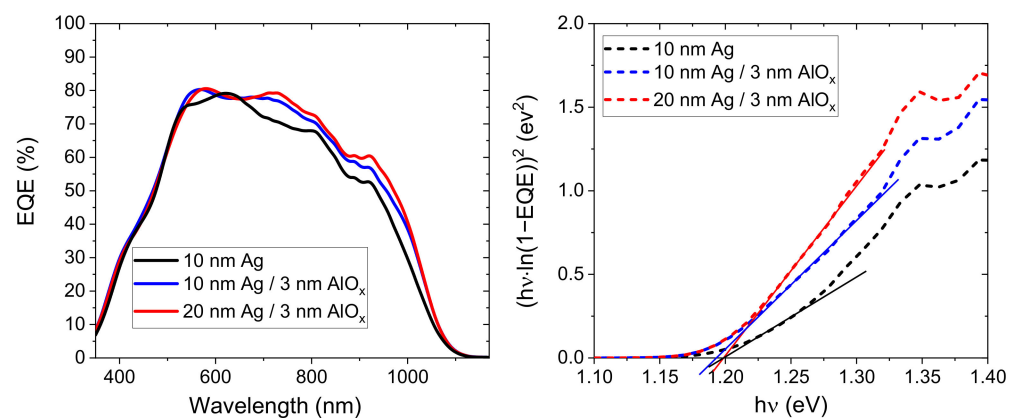
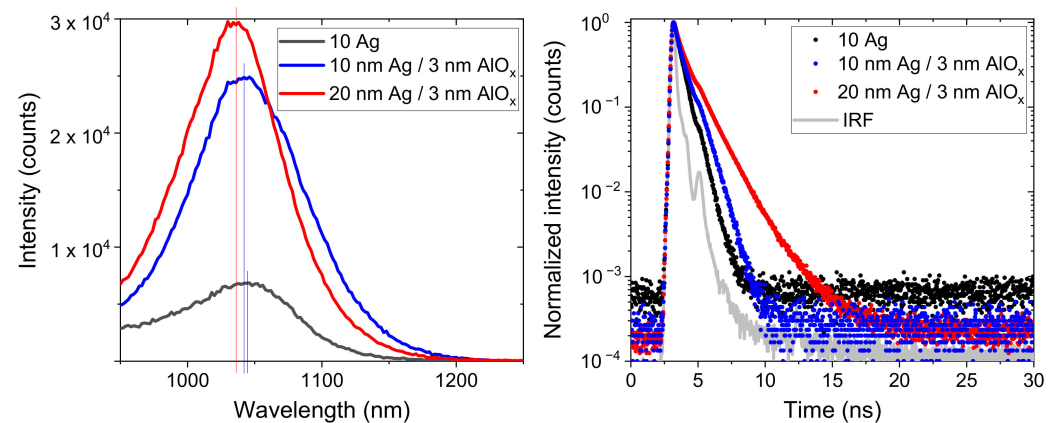


Figure 3. (Left) EQE of the Ag containing solar cells; (right) tauc plots from EQE data.

Table 1. Bandgap values from EQE and peak maxima from PL measurements.

Sample	Band Gap EQE (eV)	PL Peak Max (eV)
10 nm Ag	1.199	1.187
10 nm Ag/3 nm AlO _x	1.199	1.190
20 nm Ag/3 nm AlO _x	1.193	1.197

To gain more insight on the passivating effect of the AlO_x layer, the solar cells were measured with PL and TRPL. The results are presented in Figure 4. The PL spectra are measured under the same condition for all cells, and the intensities may be compared. For the cell without AlO_x, the measurement conditions resulted in a relatively high amount of background noise. The peak maxima are visualized with the solid lines and the corresponding energies are given in Table 1. The band gap is usually slightly below the peak maxima [23]. We find again that the peak maxima are at almost the same position for the different Ag concentrations, and with or without AlO_x. We also find that the intensity is 3–4 times higher in the presence of the AlO_x layer—this could be the effect of passivation [24]. While the PL is coming from the absorber layer, the PL yield depends on all the recombination paths. Thus, reduction of interface recombination will also increase the PL yield. TRPL decays are measured of 1040 nm emission; this is presented in Figure 4 on the right. The TRPL decays are averaged over three measurements. Also presented is the instrumental response function (IRF). We find that the decays slightly increase when AlO_x is present. In the case of 10 nm, this is only marginal, but for the 20 nm this is significant. This increase cannot be only due to AlO_x, as in that case the cells with 10 and 20 nm Ag layer with AlO_x should have similar decays. The presence of more Ag in the absorber layer also probably improves the absorber layer properties [15].

**Figure 4.** PL (left) and TRPL (right) data of Ag containing solar cells. IRF is the instrumental response function.

3.2. Elemental Profiles of Bulk and Back Contact

The elemental profiles of the complete stack of the Ag-containing solar cells were measured with ToF-SIMS. Figure 5 presents the [Ga]/([Ga] + [In])(GGI), ([Ag] + [Cu])/([Ga] + [In])(ACGI) and [Ag]/([Ag] + [Cu])(AAC) depth profiles derived from the measured counts. The counts were not calibrated. In the Figure A1, the elemental profiles are given. The profiles in Figure 5 are aligned to the CdS peak at front and at the back to the Mo signal. The Al signal is also plotted. We find that the GGI profiles are indeed rather flat; this is due to the closing of the shutter. The absorber layer is grown by stabilized elemental fluxes, which are similar to a single stage process. The Ga gradient commonly seen for a three-stage process arises from the change in the elemental fluxes during growth, which is absent in this case. The resulting GGI profile is thus rather flat.

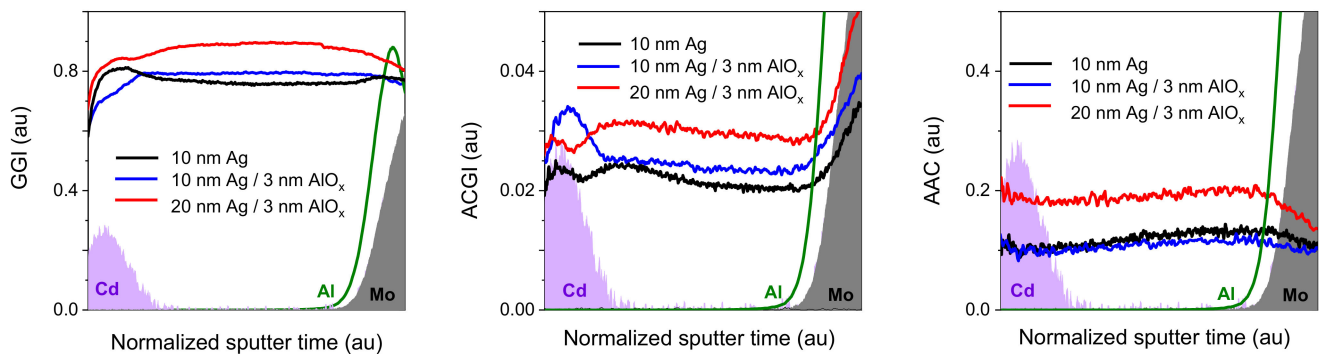


Figure 5. Non-quantified GGI, ACGI and AAC atomic ratios determined from ToF-SIMS measurements. The sputter time for each cell was adapted in such a way that the Cd and Mo signals were overlapping. Furthermore, the Al signal of the 10 nm sample is shown.

The ACGI again shows a flat profile. For all cells, the profile goes a bit up towards the front, with a steeper increase in the absence of AlO_x . This could be a real difference, as the Ag source is immediately present in this case, while in the other two situations the Ag layer is below the AlO_x , see also Figure 1. Thus, the Ag will diffuse at a later stage into the CIGS layer. The right-most figure presents the AAC profiles. Here we find that the profile of the samples with 10 nm Ag with and without AlO_x overlap, and that the AAC of the sample with 20 nm Ag is almost twice as high—this implies that almost all the Ag diffuses into the CIGS layer. A small part may still be left below the AlO_x . All the AAC profiles go slightly down towards the front, thus the AAC is a bit lower at the front than at the back. These small changes observed in the ACGI and AAC profiles towards the front are induced by the small increase of Cu towards the front (see Appendix A for the elemental profiles).

The absolute integral GGI, ACGI and AAC ratios were determined from EDS measurements for the bare absorber layers, and are presented in Table 2. The values are averaged over six different positions. The GGIs were all around 0.3. This seems in contradiction to the GGI map, though there the signals were not calibrated and thus the ratios are calculated from counts only. The AACs were about 10% and 18% for the 10 and 20 nm Ag, respectively. The silver ratio is thus far below the 27% from which variations in band gaps can be expected [25]. This change of the band gap for higher Ag amounts is due to an increased conduction band, which may cause an unfavorable band alignment with the CdS layer [26]. However, since we are below the band gap change and thus also the increase of the conduction band, it is unlikely that our cells suffer from this unfavorable band alignment. The ACGI ratios were about ~90% for the 10 nm silver layer, and close to 100% for the 20 nm silver layer. For CIGS, it is known that when the CGI ratio is close to stoichiometry, Cu_{2-x}Se phases are formed—this generally leads to shunt paths [27]. This could explain why a part of the sample with a 20 nm Ag layer had $\text{FF} < 30\%$. Thus, the three-stage process as it is requires adaptation, either in the second or third stage, to avoid the too-high ACGI ratio in the case of 20 nm Ag.

Table 2. Compositional ratios calculated from elemental concentrations measured with EDS.

Sample	GGI	ACGI	AAC
10 nm Ag	0.31 ± 0.01	0.86 ± 0.01	0.104 ± 0.003
10 nm Ag/3 nm AlO_x	0.29 ± 0.02	0.90 ± 0.04	0.100 ± 0.005
20 nm Ag/3 nm AlO_x	0.30 ± 0.01	0.99 ± 0.02	0.178 ± 0.006

SEM images from the Ag containing solar cells are presented in Figure 6. A scratch was made with a needle to obtain an image of the Mo back contact. Where the scratch was made, the Mo is visible and no difference is observed whether AlO_x was present or not. Thus, the complete stack is scratched away. At the edges, however, where the CIGS peels off and the AlO_x is not scratched away, we observe distinctively different structures at the

Mo back. We believe that these visible changes are due to some residuals of the Ag/AIO_x stack. To confirm this, the Al and Ag concentration was measured for the darker and the lighter areas with EDS. The results are presented in Figure 7. The spectra can be found in the Figure A2. For a complete analysis, the Se and In concentrations are also calculated, as these peaks partly overlap with the Al and Ag peaks. The concentrations can be found in the right graph of Figure 7. We find a clear distinguishable amount of Ag and Al between the lighter and darker areas. From the absorber layer measurements, we know that the concentration of Ag in the CIGS absorber layer is 2%, and that of In is 17%. At the back, we measure an Ag concentration that is higher than that of In. This implies that indeed some of the Ag remains below the AIO_x layer, and is not diffusing into the CIGS layer.

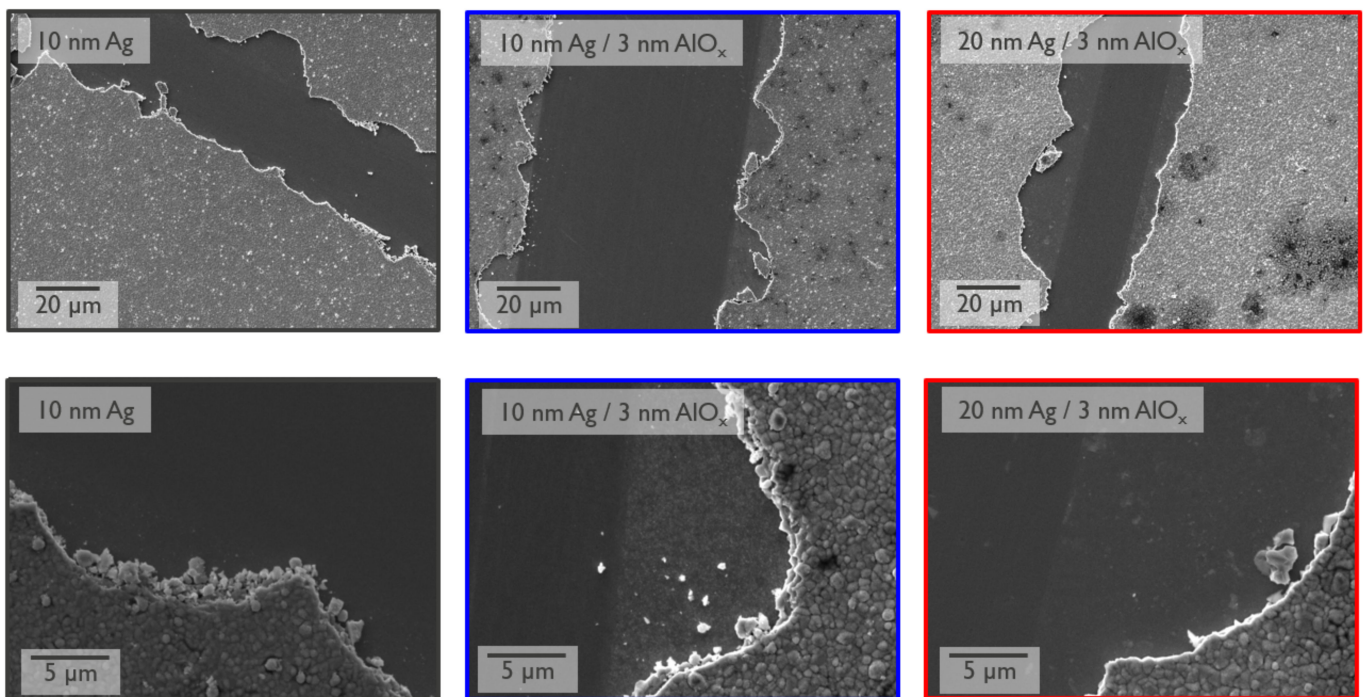


Figure 6. SEM images of the solar cell and a scratch. The scratch itself also removes the AIO_x (top), but at the edges the CIGS peels off, leaving the Ag/AIO_x back exposed (bottom).

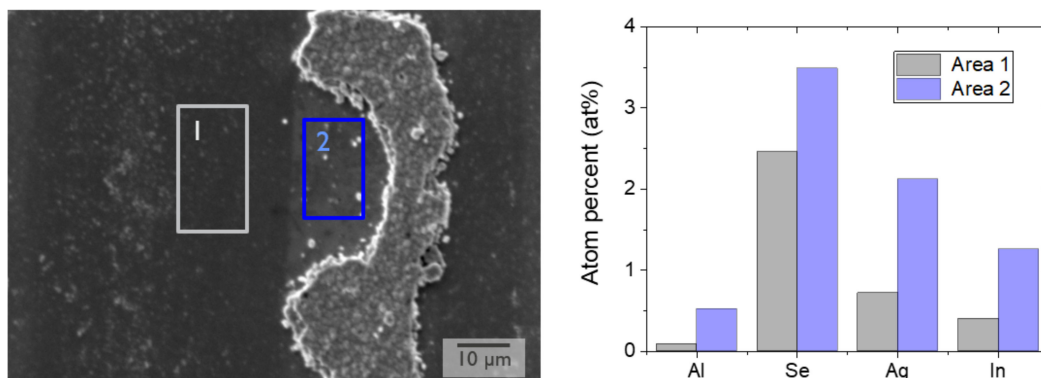


Figure 7. (Left) SEM micrograph with the areas where EDS was measured. 1: 'darker' area 2: 'lighter' area. (Right) the atomic percentages of Ag, Al, Se and In of the areas 1 and 2.

3.3. Morphology and Optical Enhancement

The presence of the Ag/AlO_x stack at the back can alter the light absorption in two ways. The first option is by increasing the reflection at the CIGS/Mo interface, due to changing the refractive index between the CIGS/Mo interface [8]. Since CIGS and Mo have closely matching refractive indices, the reflection is rather low at this interface. The Ag/AlO_x stack has a much lower refractive index, and can thus potentially increase the internal reflection, and with that the path length of the unabsorbed light. The second method to increase the path length for the longer wavelengths is by increasing the scattering properties with texturization. In an earlier contribution, we found that the formation of the contacts in the AlO_x layer happens by the accumulation of the di-electric near the etches of the contact [28]. In other words, the back contact will have a random structure with changes in height. It is likely that the presence of the Ag layer adds to these variations in height at the back contact, thus increasing the scattering properties.

To find whether the internal reflection and/or scattering properties are improved, we measured the total and diffuse reflection of the bare absorber layer. Figure 8 presents the reflection spectra. We find that the total reflection spectra are rather similar for all three samples up to 700 nm. Between 1100 and 1200 nm, the reflection of the Ag/AlO_x is slightly higher, which could indicate increased reflectance. However, the presence of the interference fringes makes it hard to be conclusive, as the amplitudes of the interference fringes vary for the different layers as well. This change in amplitude itself, though, is likely due to changes in the roughness; this can enhance the scattering properties of the layer. Figure 8 on the right presents the diffuse reflection. We find that in the presence of AlO_x, the diffuse reflection increases almost two-fold over the full wavelength range. It seems that the Ag/AlO_x stack at the back alters the morphology of the CIGS layer to such an extent that the light scattering increases.

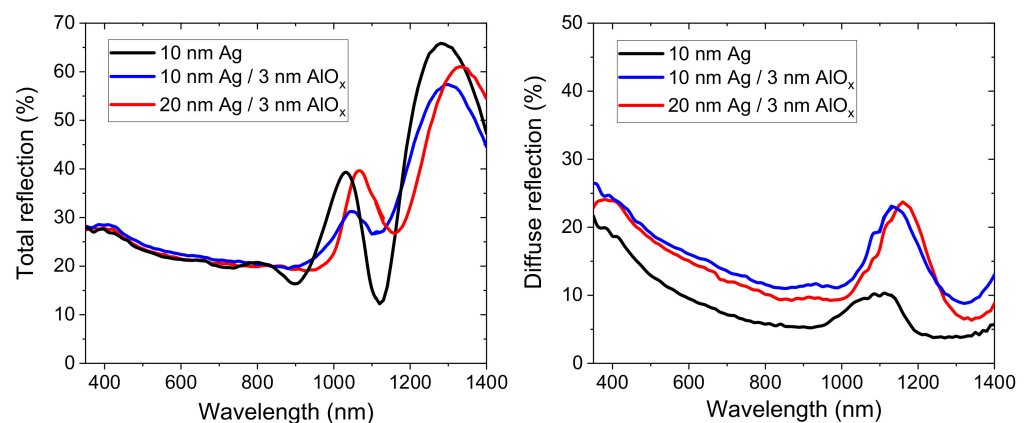


Figure 8. Total (left) and diffuse (right) reflection of the various absorber layers. In the case of the Ag/AlO_x stack at the back, the total reflection shows reduced interference amplitude and increased diffuse reflection.

Top-view images of the different absorber layers were obtained using a confocal microscope. In this way, the height is also measured and 3D figures are created using false colors for the height. These images are presented in Figure 9. It is clear that the surface is rougher in the case the CIGS is grown on the Ag/AlO_x stack. The RMS roughness was determined from these images using five line scans. We found that the roughness of the Ag reference was about 50 nm, and increased up to 80 nm for the 10 nm Ag/3 nm AlO_x absorber layer. This change in roughness could easily be responsible for the increased light absorption in the CIGS layer [29–31].

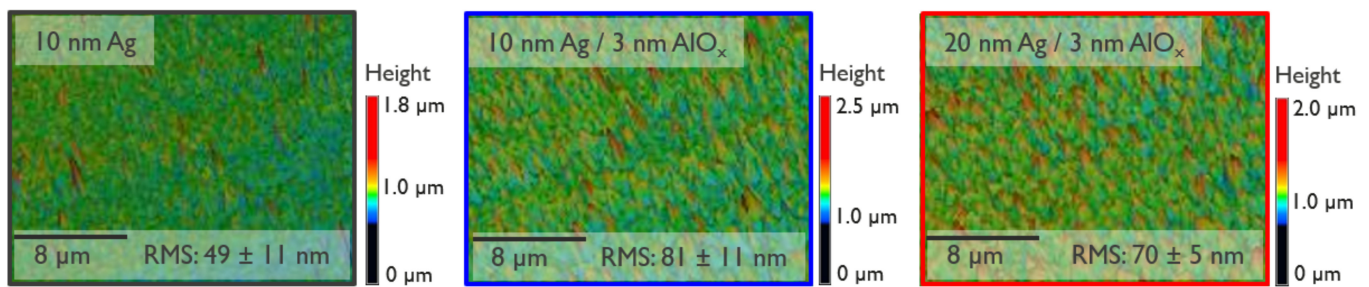


Figure 9. Confocal microscopic images of the bare absorber layers. The height variations are enhanced seven times. The given RMS values are averaged over five line measurements.

3.4. Etching

Lastly, the effect of etching was studied since we found stains in the SEM images presented in Figure 6. Furthermore, the addition of Ag could possibly lead to secondary phases [32]. While this tends to occur only at higher AAC and GGI ratios, it has to be noted that we start with an Ag layer, and thus a very high AAC. It is therefore possible that the stains are due to some secondary phases or segregation. The EDS did not reveal compositional changes, making it likely that it is only at the surface. We applied a $S(NH_4)_2$ etching step, which is already known to selectively remove copper selenide phase, and to improve the surface generally [18,33]. Two samples with 10 nm Ag and 3 nm AlO_x were prepared, of which one sample was etched. The absorber layer was rinsed in water prior to further solar cell processing. The JV parameters are presented in Figure 10, and the best JV curves with its parameters are presented in Figure 11. Without etching, the efficiency was about 9% on average, similar to those presented in Figure 2. This shows the repeatability. After etching, we find that all solar cell parameters are improved. This is clearly an indication that the efficiency was limited by defects at the front surface. The efficiency increased to almost 11% on average, with the most efficient cell having an efficiency of 11.7%.

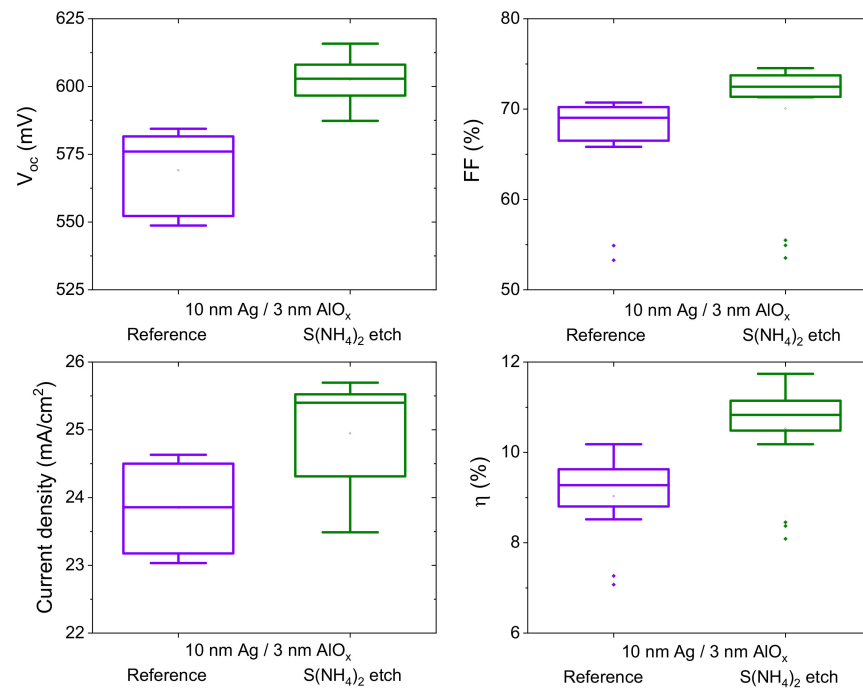


Figure 10. JV parameters of Ag/ AlO_x back reflector with and without ammonia sulfide etching.

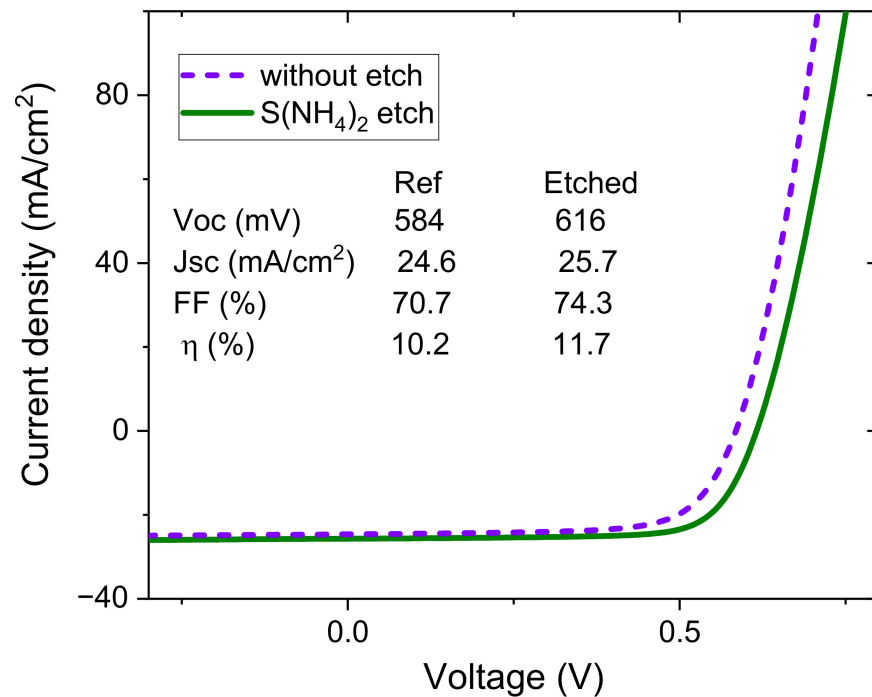


Figure 11. JV curves and parameters of the best solar cells.

4. Conclusions

Ultrathin CIGS solar cells were prepared on a thin Ag/AIO_x stack. The CIGS layers were grown by a three-stage co-evaporation process, and the Ag diffused into the CIGS layer during the growth. This was confirmed by measuring the depth profiles with ToF-SIMS. No difference in Ag content in the presence of AIO_x or not was measured for the samples with 10 nm Ag. The improvements in the presence of AIO_x were substantial, and an increased efficiency from about 7% to 9% was measured. All solar cell parameters were improved, which was attributed to a combined effect of passivation and optical enhancement. With SEM, images of the Mo back contact were made, and a thin structured layer was seen in the presence of the Ag/AIO_x back contact. With EDS, residuals of Al and Ag were measured. This Ag/AIO_x stack seems to induce an increase in roughness, and thereby light scattering. At the front, darker and lighter spots in the SEM images were observed in the case AIO_x was present. Even though these cells had the best performance, it is an indication of losses. When etching the absorber layer in ammonia sulfide prior to further solar cell processing, the efficiency increased even further to 11% on average. The results reveal a simple method to apply both passivation and optical structures at the back without adding losses.

Author Contributions: Conceptualization, B.V. and J.d.W.; methodology, G.B. (Gizem Birant) and J.d.W.; software, G.B. (Guy Brammertz); formal analysis, J.d.W.; writing—original draft preparation, J.d.W.; writing—review and editing, J.d.W. and B.V.; project administration, M.M. and J.P.; and funding acquisition, B.V. All authors have read and agreed to the published version of the manuscript.

Funding: This research was funded by European Union H2020 research and innovation program grant number 715027.

Institutional Review Board Statement: Not applicable.

Informed Consent Statement: Not applicable.

Data Availability Statement: The data presented in this study are available upon request from the corresponding author.

Conflicts of Interest: The authors declare no conflict of interest.

Appendix A

TOF-SIMS elemental profiles of the 3 Ag-containing sample.

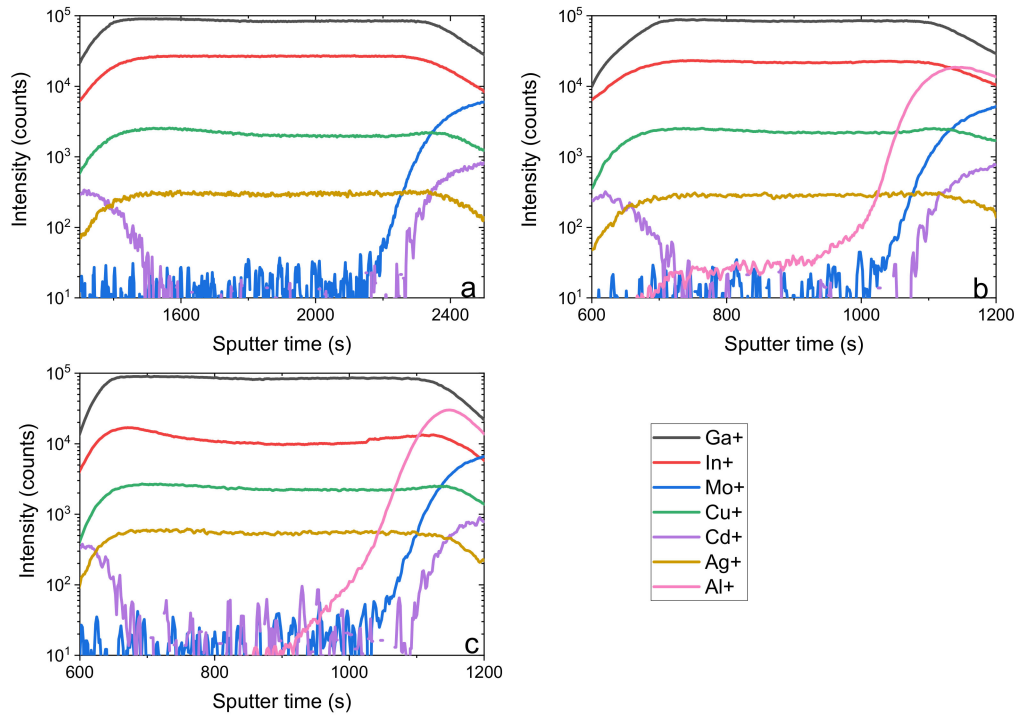


Figure A1. Elemental profiles of the 3 Ag-containing solar cells. (a) 10 nm Ag; (b) 10 nm Ag/3 nm AlO_x; and (c) 20 nm Ag/3 nm AlO_x.

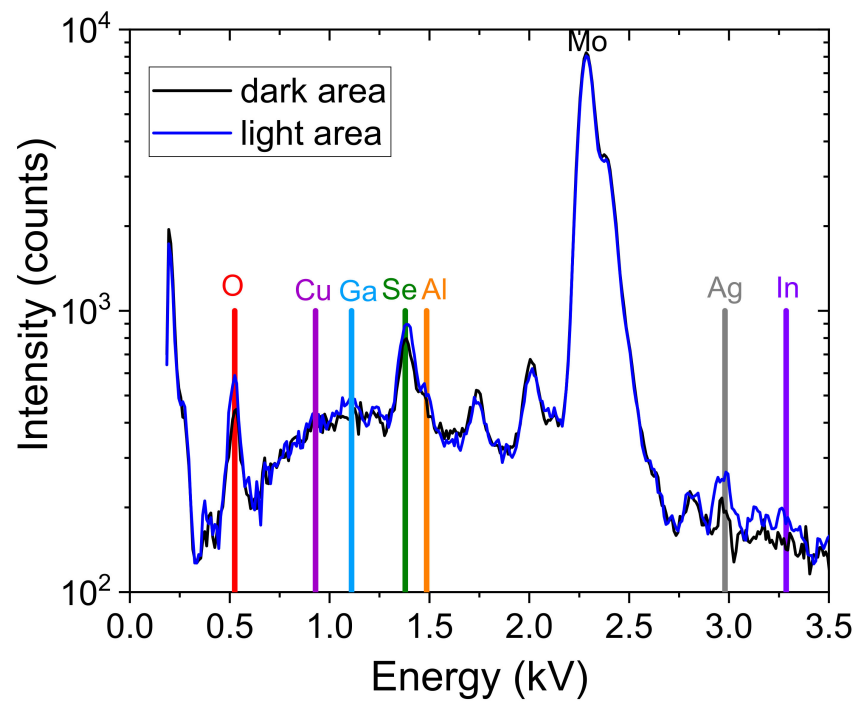


Figure A2. EDS spectra of the Mo back contact with the assigned peak positions: Al, Ag, In and Se. Also shown are O, Ga, Cu and Mo.

References

1. Mansfield, L.M.; Kanevce, A.; Harvey, S.P.; Bowers, K.; Beall, C.; Glynn, S.; Repins, I.L. Efficiency increased to 15.2% for ultra-thin Cu(In,Ga)Se₂ solar cells. *Prog. Photovolt. Res. Appl.* **2018**, *26*, 949–954. [[CrossRef](#)]
2. Birant, G.; de Wild, J.; Meuris, M.; Poortmans, J.; Vermang, B. Dielectric-based rear surface passivation approaches for Cu(In,Ga)Se₂ solar cells—A review. *Appl. Sci.* **2019**, *9*, 677. [[CrossRef](#)]
3. Vermang, B.; Fjällström, V.; Gao, X.; Edoff, M. Improved Rear Surface Passivation of Cu(In,Ga)Se₂ Solar Cells: A Combination of an Al₂O₃ Rear Surface Passivation Layer and Nanosized Local Rear Point Contacts. *IEEE J. Photovolt.* **2014**, *4*, 486–492. [[CrossRef](#)]
4. Haug, F.-J.; Ballif, C. Light management in thin film silicon solar cells. *Energy Environ. Sci.* **2015**, *8*, 824–837. [[CrossRef](#)]
5. Pfeffer, F.; Eisenlohr, J.; Basch, A.; Hermle, M.; Lee, B.G.; Goldschmidt, J.C. Systematic analysis of diffuse rear reflectors for enhanced light trapping in silicon solar cells. *Sol. Energy Mater. Sol. Cells* **2016**, *152*, 80–86. [[CrossRef](#)]
6. Ferry, V.E.; Sweatlock, L.A.; Pacifici, D.; Atwater, H.A. Plasmonic Nanostructure Design for Efficient Light Coupling into Solar Cells. *Nano Lett.* **2008**, *8*, 4391–4397. [[CrossRef](#)]
7. Vermang, B.; Wätjen, J.T.; Fjällström, V.; Rostvall, F.; Edoff, M.; Kotipalli, R.; Henry, F.; Flandre, D. Employing Si solar cell technology to increase efficiency of ultra-thin Cu(In,Ga)Se₂ solar cells. *Prog. Photovolt. Res. Appl.* **2014**, *22*, 1023–1029. [[CrossRef](#)] [[PubMed](#)]
8. Kovacic, M.; Krc, J.; Lipovsek, B.; Chen, W.-C.; Edoff, M.; Bolt, P.J.; van Deelen, J.; Zhukova, M.; Lontchi, J.; Flandre, D.; et al. Light management design in ultra-thin chalcopyrite photovoltaic devices by employing optical modelling. *Sol. Energy Mater. Sol. Cells* **2019**, *200*, 109933. [[CrossRef](#)]
9. Van Lare, C.; Yin, G.; Polman, A.; Schmid, M. Light Coupling and Trapping in Ultrathin Cu(In,Ga)Se₂ Solar Cells Using Dielectric Scattering Patterns. *ACS Nano* **2015**, *9*, 9603–9613. [[CrossRef](#)]
10. Schneider, T.; Tröndle, J.; Fuhrmann, B.; Syrowatka, F.; Sprafke, A.; Scheer, R. Ultrathin CIGSe Solar Cells with Integrated Structured Back Reflector. *Sol. RRL* **2020**, *4*, 2000295. [[CrossRef](#)]
11. Naghavi, N.; Mollica, F.; Goffard, J.; Posada, J.; Duchatelet, A.; Jubault, M.; Donsanti, F.; Cattoni, A.; Collin, S.; Grand, P.P.; et al. Ultrathin Cu(In,Ga)Se₂ based solar cells. *Thin Solid Films* **2017**, *633*, 55–60. [[CrossRef](#)]
12. Gouillart, L.; Cattoni, A.; Chen, W.-C.; Goffard, J.; Riekehr, L.; Keller, J.; Jubault, M.; Naghavi, N.; Edoff, M.; Collin, S. Interface engineering of ultrathin Cu(In,Ga)Se₂ solar cells on reflective back contacts. *Prog. Photovolt. Res. Appl.* **2021**, *29*, 212–221. [[CrossRef](#)]
13. Mollica, F.; Jubault, M.; Donsanti, F.; Loubat, A.; Bouttemy, M.; Etcheberry, A.; Naghavi, N. Light absorption enhancement in ultra-thin Cu(In,Ga)Se₂ solar cells by substituting the back-contact with a transparent conducting oxide based reflector. *Thin Solid Films* **2017**, *633*, 202–207. [[CrossRef](#)]
14. Oliveira, A.J.N.; de Wild, J.; Oliveira, K.; Valença, B.A.; Teixeira, J.P.; Guerreiro, J.R.L.; Abalde-Cela, S.; Lopes, T.S.; Ribeiro, R.M.; Cunha, J.M.V.; et al. Encapsulation of Nanostructures in a Dielectric Matrix Providing Optical Enhancement in Ultrathin Solar Cells. *Sol. RRL* **2020**, *4*, 2000310. [[CrossRef](#)]
15. Erslev, P.T.; Lee, J.; Hanket, G.M.; Shafarman, W.N.; Cohen, J.D. The electronic structure of Cu(In_{1-x}Ga_x)Se₂ alloyed with silver. *Thin Solid Films* **2011**, *519*, 7296–7299. [[CrossRef](#)]
16. Ledinek, D.; Donzel-Gargand, O.; Sköld, M.; Keller, J.; Edoff, M. Effect of different Na supply methods on thin Cu(In,Ga)Se₂ solar cells with Al₂O₃ rear passivation layers. *Sol. Energy Mater. Sol. Cells* **2018**, *187*, 160–169. [[CrossRef](#)]
17. Birant, G.; de Wild, J.; Kohl, T.; Buldu, D.G.; Brammertz, G.; Meuris, M.; Poortmans, J.; Vermang, B. Innovative and industrially viable approach to fabricate AlO_x rear passivated ultra-thin Cu(In, Ga)Se₂ (CIGS) solar cells. *Sol. Energy* **2020**, *207*, 1002–1008. [[CrossRef](#)]
18. Buffière, M.; Mel, A.-A.E.; Lenaers, N.; Brammertz, G.; Zaghi, A.E.; Meuris, M.; Poortmans, J. Surface Cleaning and Passivation Using (NH₄)₂S Treatment for Cu(In,Ga)Se₂ Solar Cells: A Safe Alternative to KCN. *Adv. Energy Mater.* **2015**, *5*, 1401689. [[CrossRef](#)]
19. De Wild, J.; Buldu, D.G.; Schnabel, T.; Simor, M.; Kohl, T.; Birant, G.; Brammertz, G.; Meuris, M.; Poortmans, J.; Vermang, B. High Voc upon KF Post-Deposition Treatment for Ultrathin Single-Stage Coevaporated Cu(In, Ga)Se₂ Solar Cells. *ACS Appl. Energy Mater.* **2019**, *2*, 6102–6111. [[CrossRef](#)]
20. Edoff, M.; Jarmar, T.; Nilsson, N.S.; Wallin, E.; Höglström, D.; Stolt, O.; Lundberg, O.; Shafarman, W.; Stolt, L. High Voc in (Cu,Ag)(In,Ga)Se₂ Solar Cells. *IEEE J. Photovolt.* **2017**, *7*, 1789–1794. [[CrossRef](#)]
21. Valdes, N.; Lee, J.; Shafarman, W. Comparison of Ag and Ga alloying in low bandgap CuInSe₂-based solar cells. *Sol. Energy Mater. Sol. Cells* **2019**, *195*, 155–159. [[CrossRef](#)]
22. Suresh, S.; de Wild, J.; Kohl, T.; Buldu, D.G.; Brammertz, G.; Meuris, M.; Poortmans, J.; Isabella, O.; Zeman, M.; Vermang, B. A study to improve light confinement and rear-surface passivation in a thin-Cu(In, Ga)Se₂ solar cell. *Thin Solid Films* **2019**, *669*, 399–403. [[CrossRef](#)]
23. Siebentritt, S. Shallow Defects in the Wide Gap Chalcopyrite CuGaSe₂. In *Wide-Gap Chalcopyrites*; Siebentritt, S., Rau, U., Eds.; Springer Series in Materials Science; Springer: Berlin/Heidelberg, Germany, 2006; pp. 113–156. ISBN 978-3-540-31293-2.
24. Luo, S.; Eisler, C.; Wong, T.-H.; Xiao, H.; Lin, C.-E.; Wu, T.-T.; Shen, C.-H.; Shieh, J.-M.; Tsai, C.-C.; Liu, C.-W.; et al. Suppression of surface recombination in CuInSe₂ (CIS) thin films via Trioctylphosphine Sulfide (TOP:S) surface passivation. *Acta Mater.* **2016**, *106*, 171–181. [[CrossRef](#)]
25. Boyle, J.H.; McCandless, B.E.; Shafarman, W.N.; Birkmire, R.W. Structural and optical properties of (Ag,Cu)(In,Ga)Se₂ polycrystalline thin film alloys. *J. Appl. Phys.* **2014**, *115*, 223504. [[CrossRef](#)]

26. Keller, J.; Sopiha, K.V.; Stolt, O.; Stolt, L.; Persson, C.; Scragg, J.J.S.; Törndahl, T.; Edoff, M. Wide-gap (Ag,Cu)(In,Ga)Se₂ solar cells with different buffer materials—A path to a better heterojunction. *Prog. Photovolt. Res. Appl.* **2020**, *28*, 237–250. [[CrossRef](#)]
27. Virtuani, A.; Lotter, E.; Powalla, M.; Rau, U.; Werner, J.H.; Acciarri, M. Influence of Cu content on electronic transport and shunting behavior of Cu(In,Ga)Se₂ solar cells. *J. Appl. Phys.* **2006**, *99*, 014906. [[CrossRef](#)]
28. Kandybka, I.; Birant, G.; de Wild, J.; Buldu, D.G.; Kohl, T.; Eachambadi, R.T.; Brammertz, G.; Manca, J.V.; Meuris, M.; Poortmans, J.; et al. Novel cost-effective approach to produce nano-sized contact openings in an aluminum oxide passivation layer up to 30 nm thick for CIGS solar cells. *J. Phys. D Appl. Phys.* **2021**, *54*, 234004. [[CrossRef](#)]
29. Zeman, M.; van Swaaij, R.A.C.M.M.; Metselaar, J.W.; Schropp, R.E.I. Optical modeling of a-Si:H solar cells with rough interfaces: Effect of back contact and interface roughness. *J. Appl. Phys.* **2000**, *88*, 6436–6443. [[CrossRef](#)]
30. Jehl, Z.; Bouttemy, M.; Lincot, D.; Guillemoles, J.F.; Gerard, I.; Etcheberry, A.; Voorwinden, G.; Powalla, M.; Naghavi, N. Insights on the influence of surface roughness on photovoltaic properties of state of the art copper indium gallium diselenide thin films solar cells. *J. Appl. Phys.* **2012**, *111*, 114509. [[CrossRef](#)]
31. Scholtz, L.; Ladanyi, L.; Mullerova, J. Influence of Surface Roughness on Optical Characteristics of Multilayer Solar Cells. *Adv. Electr. Electron. Eng.* **2014**, *12*, 631–638. [[CrossRef](#)]
32. Chen, L.; Soltanmohammad, S.; Lee, J.; McCandless, B.E.; Shafarman, W.N. Secondary phase formation in (Ag,Cu)(In,Ga)Se₂ thin films grown by three-stage co-evaporation. *Sol. Energy Mater. Sol. Cells* **2017**, *166*, 18–26. [[CrossRef](#)]
33. Buldu, D.G.; de Wild, J.; Kohl, T.; Brammertz, G.; Birant, G.; Meuris, M.; Poortmans, J.; Vermang, B. Study of Ammonium Sulfide Surface Treatment for Ultrathin Cu(In,Ga)Se₂ with Different Cu/(Ga + In) Ratios. *Phys. Status Solidi A* **2020**, *217*, 2000307. [[CrossRef](#)]